Multifluid flows in a vertical channel undergoing topology changes: Effect of void fraction

Jiacai Lu[*] and Gretar Tryggvason[†]
Department of Mechanical Engineering, Johns Hopkins University, Baltimore, Maryland 21218, USA

(Received 21 March 2019; published 12 August 2019)

The effect of void fraction on turbulent multifluid flows undergoing topology changes in a vertical channel is examined by numerical simulations using a front tracking and finite volume method. Several blobs or bubbles of the light fluid are initially placed in a turbulent channel flow. When the blobs collide and the liquid film between them becomes very thin it is ruptured, and the blobs are allowed to coalesce. The rupture is done for a predetermined film thickness selected in such a way that the results are relatively insensitive to its exact value. For the parameters used here, the blobs generally break up after the initial coalescence, and five simulations for void fractions from about 5% to 25% are carried out until the flow has reached an approximately steady state. The evolution of various integral quantities, such as the average flow rate, wall shear, and interface area, are monitored and compared. Various averages of the flow field and the phase distribution, over planes parallel to the walls, are then examined at late times, when the flow has reached an approximate statistically steady state. At steady state, the probability distribution of blob volumes is similar, and the light fluid is contained in blobs with an average Eötvös number of about 3.5, for all the void fractions. However, the deformation and the surface area of the largest blobs are much larger for the higher void fractions, suggesting that the flow starts to depart from the bubbly regime at a void fraction of about 15%.

DOI: 10.1103/PhysRevFluids.4.084301

I. INTRODUCTION

Considerable effort has been devoted to studies of bubbly flows using direct numerical simulations (DNS) for the last two decades or so [1–9]. For channel flows results are now available for hundreds of bubbles and relatively large Reynolds numbers, such as in Refs. [10,11], where the motion of 571 bubbles of various sizes was simulated for a friction Reynolds number of $\mathrm{Re}^{+} = 500$ (corresponding to a channel Reynolds number of about 24 000). Such simulations have yielded significant insight into the dynamics of bubbly flows, including how the void fraction distribution depends on the deformability of the bubbles and the flow directions. For an overview of recent progress in DNS studies of bubbly flows, see the recent review article by Elghobashi [12]. Those results are currently being used to help improve conventional models of the average multiphase flows at scales that cannot easily be followed using DNS [13–15], as well as for exploring new modeling strategies [16,17]. Bubbly flows are, however, mostly seen for relatively low void fractions, and even in cases where the flow consists predominantly of bubbles, the flow is often more complex due to transient coalescence and breakup. For sufficiently high void fractions the fluids are so intermingled that it is difficult to identify distinct bubbles (or drops).

[*]jiacai.lu@jhu.edu
[†]gtryggv1@jhu.edu

Experimental studies of multiphase flow in vertical pipes include Refs. [18–21] for adiabatic flows. Other authors have studied the effect of surfactants [22] and flashing flows [23], for example. As the void fraction increases, the flow characteristics change in fundamental ways as the flow transitions from one regime to another, and many authors have presented maps that show the boundary between the different regimes as functions of the governing parameters. Early proposals can be found in Refs. [24,25], and a brief overview of the different maps that have been proposed is given in Ref. [26]. For a review of experiments and modeling of air liquid flows in vertical pipes, with a focus on gas-lift pumps for oil recovery, see Ref. [27], for example. Modeling flow regime transitions is, however, still very primitive and based mostly on experimental results and scaling considerations. So far little has been done to use DNS to cast light on the various processes governing the flow in regimes beyond bubbly flows.

In Ref. [28] we examined the evolution of flows initially consisting of several bubbles in a turbulent channel at a sufficiently high void fraction so that the bubbles collide and the liquid film between them becomes very thin. This film was ruptured at a predetermined thickness, and the bubbles were allowed to coalesce. The focus was on the effect of surface tension, and for high surface tension the bubbles continued to coalesce, eventually forming one large bubble. At low surface tension, on the other hand, the large bubbles broke up again, sometimes undergoing repeated coalescence and breakup. The evolution of various integral quantities, such as the average flow rate, wall shear, and interface area, was monitored and compared for different governing parameters, as well as averages of the flow field and the phase distribution over planes parallel to the walls. The microstructure of one case, at statistically steady state, was examined in some detail, using low-order probability functions. In the present paper we continue to examine multifluid channel flows undergoing repeated topological changes but focus on the effect of the void fraction, keeping all other parameters constant. We do, in particular, examine how the size and shape distribution of blobs of the light fluid, as well as the frequency of topology changes, depend on the void fraction, and for what void fraction range the flow can reasonably be classified as bubbly flow.

II. GOVERNING EQUATIONS AND NUMERICAL METHOD

We examine the flow in a vertical rectangular channel, where two immiscible fluids, a light and a heavy one, are driven upward by an imposed pressure gradient. Thus, we write the pressure gradient as a sum of the imposed pressure gradient $(dP_0/dx)\mathbf{k}$, where $\mathbf{k}$ is a unit vector in the vertical direction, x, and the pressure needed to make sure the flow is incompressible, $\nabla p'$. Although the full pressure changes from one end of the computational domain to the other end in the flow direction, $\nabla p'$ can be assumed to be periodic. By adding and subtracting the weight of the mixture, the "one-fluid" Navier-Stokes equations are

$$\frac{\partial \rho \mathbf{u}}{\partial t} + \nabla \cdot (\rho \mathbf{u}\mathbf{u}) = -\nabla p' - \beta \mathbf{k} - (\rho - \rho_{av}) g \mathbf{k} + \nabla \cdot \mu (\nabla \mathbf{u} + \nabla \mathbf{u}^T) + \sigma \int_F \kappa_f \mathbf{n}_f \delta(\mathbf{x} - \mathbf{x}_f)\, dA_f, \tag{1}$$

which describe the flow in the whole computational domain. The singular last term is the surface tension, which is concentrated at the fluid interface. Here $\mathbf{u}$ is the velocity vector, ρ and μ are the discontinuous density and viscosity fields, respectively, g is the gravity acceleration, and σ is the constant surface tension. δ is a three-dimensional delta function constructed by repeated multiplication of one-dimensional delta functions, κ_f is twice the mean curvature, $\mathbf{n}_f$ is a unit vector normal to the front, $\mathbf{x}$ is the point at which the equation is evaluated, and $\mathbf{x}_f$ is the position of the front. In addition to the momentum equations we need the incompressibility conditions $\nabla \cdot \mathbf{u} = 0$, which leads to a nonseparable elliptic equation for the pressure. Here

$$\beta = \frac{dP_0}{dx} + \rho_{av} g, \tag{2}$$

where ρ_{av} is the average weight of the mixture in the whole channel. At steady state, the wall shear τ_w balances the imposed pressure gradient and the weight of the mixture so we must have $\tau_w = h\beta$, where h is the half width of the channel. In our simulations we keep β constant when we change the void fraction and thus ρ_{av}.

The equations are solved on a regular structured staggered grid, using a front-tracking and finite-volume method. Time integration is done by a second-order predictor-corrector method, the advection terms are approximated using a QUICK scheme, and the viscous terms are discretized by second-order centered differences. The pressure equation is solved using a multigrid method in HYPRE [29] to enforce a divergence-free velocity field. The fluid interface is tracked by connected marker points (referred to as the "front") to advect the density and the viscosity fields and to accurately compute the surface tension. The front points are connected into an unstructured surface grid that is advected by the fluid velocity, interpolated from the fixed grid. As the front stretches and deforms, surface markers are dynamically added and deleted as needed. The surface tension is represented as a singular distribution (delta functions) at the front. The gradient of the indicator function (delta function when the change is abrupt across the interface) and the singular surface force are transferred to the fixed grid by approximating the singular distributions by compact but smooth functions on the grid. After the front has been advected, the density and the viscosity fields are reconstructed by integration of the smooth grid-delta function and the surface tension added to the nodal values of the discrete Navier-Stokes equations. The method is not completely volume conserving, and we therefore adjust the volume at each time step by moving the interfaces slightly in the normal direction. In all cases these adjustments are very minor. The method was introduced in Ref. [30] and has been tested and validated in a number of ways. The necessary grid resolution varies with the governing parameters of the problem and finer resolution is generally required for high Reynolds number flows compared to low Reynolds number flows, as in other numerical simulations. We have applied the method to a large range of multiphase flows, and studies of bubbly flows include Refs. [3,6,31,32]. Implementation of similar ideas by other researchers and applications to bubbly flows can be found in Refs. [4,5,9,13,33–36], for example.

Topology changes in multiphase flows take place as films rupture and threads break. Methods that track an indicator function identifying the different phases directly on an Eularian grid (such as volume of fluid (VOF) or level set methods) will produce topology change when the resolution of a film or a thread is comparable to the grid spacing, but methods that use connected marker points to track the interface generally will not yield a change in topology. Both methods can, of course, be modified to either allow or prevent topology changes. Thin threads that break are by far the easier to deal with. The Navier-Stokes equations predict that the diameter of threads becomes zero in a finite time, and no additional physical modeling needs to be included. The breakup is also fast, and although the thread may not be well resolved just before it breaks, this is usually such a short time that it does not have a significant effect on the overall dynamics of the flow. Most methods generally handle thread breakup easily. The thickness of thin films, on the other hand, usually does not go to zero in a finite time, according to the standard Navier-Stokes equations, and we need to introduce additional processes to account for rupture. In reality, instabilities due to short-range attractive forces lead to a hole that grows by retreat and breakup. Short-range forces are, however, usually not included in simulations of multiphase flows, and in simulations by methods that track the marker function directly, such as VOF or level set methods, rupture takes place when the film is no longer resolved. In many cases results produced by such methods look "plausible," but in other cases the grid dependency of the rupture prevents convergence under grid refinement. When the interface is tracked by connected markers, as here, the default behavior is no rupture, and if rupture is desired, that must be explicitly added to the method.

In the simulations discussed here the topology change is accomplished by reconnecting fronts that are closer than a prescribed minimum distance. The topology change algorithm consists of first identifying close front points and then restructuring the front. To identify close points we divide the domain into subdomains and construct a linked list of points in each domain so that we can limit the search to points in each subdomain. Once close points have been identified, we merge all close

TABLE I. Parameter list for all cases for effect of surface tension.

	Case 1	Case 2	Case 3	Case 4	Case 5	Case 6
Initial bubble diameter	0.5	0.5	0.5	0.5	0.5	0.25
Initial number of bubbles	8	15	23	31	38	64
Void fraction (α)	5.31%	9.95%	15.25%	20.56%	25.20%	5.31%

points and eliminate elements between merged points. In the actual code, we have implemented a number of steps to increase the efficiency of the topology change, but none of these steps affect the eventual outcome.

In our earlier paper [28], we examined in some detail how coalescence criteria and resolution affected the results for flows undergoing repeated topology changes and found that for a range of parameters the results were relatively insensitive to the exact value. We believe that the flow examined here will show a similar insensitivity. While the question of how important it is to incorporate the full physics responsible for the rupture of thin films and to resolve small-scale features is obviously not a fully settled issue, we believe that the approach taken here approximates the evolution of a real two-fluid system fairly well and that the aspects that we emphasize are relevant to real systems.

III. PROBLEM SETUP

Our computational domain is a rectangular channel, bounded by two parallel vertical walls, and with periodic boundaries in the streamwise and spanwise directions. In computational units the domain size is $\pi \times 0.5\pi \times 2$ in the streamwise (X), spanwise (Z), and wall-normal (Y) direction. The flow is driven upward by an imposed pressure gradient, and the initial velocity field is a stationary turbulent flow with a friction Reynolds number of 150. The density of the heavy fluid is $\rho_l = 1.0$, and the density of the light fluid is $\rho_g = 0.1$. The heavy and the light fluid viscosities are both $\mu_{l,g} = 2.5 \times 10^{-4}$, and gravity is $g = 0.1$, acting in the negative X direction. Surface tension is $\sigma = 0.002$. The initial turbulent flow is generated using a spectral code [37,38], and the bubbles are simply placed in the flow at time zero, requiring the flow to adjust to the bubbles in the first few time steps. Using an initially turbulent flow ensures that the bubbles collide with each other.

The Morton number is $\mathrm{Mo} = \Delta\rho g\mu^4/\rho^2\sigma^3 = 4.4 \times 10^{-8}$. The nondimensional pressure gradient is $\beta/\Delta\rho g = 0.0156$, and the Eötvös number based on the channel width is $\mathrm{Eo} = \Delta\rho g D^2/\sigma = 180$, where $D = 2$ is the width of the channel. Instead of the Eötvös number we could also use the Archimedes number $\mathrm{Ar} = \rho\Delta\rho g D^3/\mu^2 = 1.15 \times 10^7$. We use the channel width in the Eötvös and the Archimedes numbers since the eventual diameter of the bubbles is not prescribed. If we assume that it is likely that the bubbles will coalesce and breakup in such a way that bubbles with Eötvös number based on diameter equal to unity are likely to appear, then the diameter of those bubbles would be $d_{1.0} = \sqrt{\sigma/\Delta\rho g} = 0.149$. According to a well-known chart in Ref. [39], bubbles with $\mathrm{Eo} = 1$ should be slightly deformed. We note that in our earlier paper [28] the friction Reynolds number was 128, and the void fraction was 13.58%. The high void fractions examined here lead to much more frequent and complex topology changes.

The objective of the present investigation is to examine how the flow structure changes with void fraction, and to do so we conduct a series of simulations where all parameters have been kept constant except for the void fraction. Initially, a number of relatively large bubbles with a diameter of 0.5 are placed randomly in the channel. The number of bubbles is varied to give different void fractions. The initial number of bubbles, their diameters, and the void fraction α for each case are listed in Table I. In one case (Case 6), we also did a simulation starting with a larger number of smaller bubbles, but with void fraction and all other parameters equal to Case 1, to confirm that the evolution at later times is independent of the initial conditions. The computational domain is

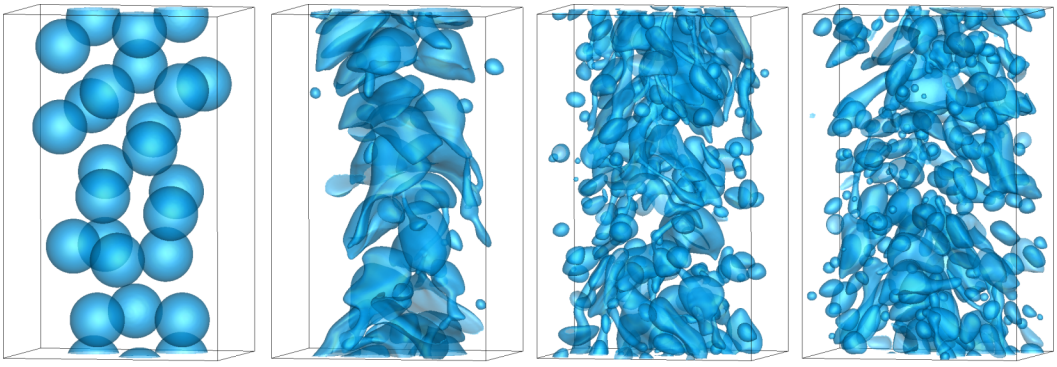

FIG. 1. Four frames showing the fluid interface for early times of 0.0 (a), 10.0 (b), 20.0 (c), and 30.0 (d), for void fraction equal to 15.25% (Case 3).

resolved by a grid that is 192 (uniform) × 96 (uniform) × 128 (nonuniform) cells. The smallest and biggest cell sizes in the wall-normal direction are 0.003549 and 0.023 in computational units. The interfaces undergo topology changes when the distance between two distinct interfaces is less than $0.32\Delta x = 0.005236$ [28]. We present all results in computational, rather than nondimensional units, to reduce the probability of error or misinterpretation.

IV. RESULTS

A. Transient evolution

The interface separating the light and the heavy fluid is shown in Fig. 1 for a void fraction equal to 15.25% (Case 3), at the initial time and three subsequent early times. The surface tension here is sufficiently small so the initially spherical bubbles start to deform, break up, and coalesce almost immediately, and even in the second frame we see that bubbles much smaller than the original ones have formed. The interfaces continue to deform, and in the third and fourth frames we see both large and small bubbles. While there is an obvious difference between the interface structure in the second and the third frames, in the third and the forth frames the overall structure appears to be more similar, suggesting that the shape of the interface is reaching a statistically stationary state. Notice that there is almost no accumulation of bubbles at the channel walls, indicating that most of the bubbles are deformed and haver a small or negative lift coefficient [40].

The time evolution of various quantities averaged over the whole channel is shown in Fig. 2. The top frame shows the phase-averaged velocity of the heavy fluid (“liquid”), and the middle frame shows the phase-averaged velocity of the light fluid (“gas”). For the lowest void fractions the velocities very quickly settle down to a nearly constant value. The gas velocity initially shows a spike as the flow adjusts to the presence of the bubbles and then fluctuates more than the liquid velocity. The velocities for the two lowest void fractions (5.31% and 9.94%—Cases 1 and 2) are essentially identical, and the profile for void fraction 15.31% (Case 3) is just slight larger. For void fraction 20.56% (Case 4) the velocities are still higher and increase slightly with time, particularly the liquid velocity. For void fraction 25.20% (Case 5) the velocity is highest and continues to rise with time. The average wall shear stress is shown in the bottom frame. At time zero, as well as once the flow reaches a statistically stationary state, the pressure gradient driving the flow and the weight of the mixture balance the wall shear. As the bubbles are inserted the buoyancy causes a transient drop in the wall shear, but the flow then adjusts to the presence of the light fluid, and for the lower void fraction cases the wall shear fluctuates around the equilibrium value. For the highest void fraction the wall shear continues to grow. The figure suggests that the lowest void fraction cases

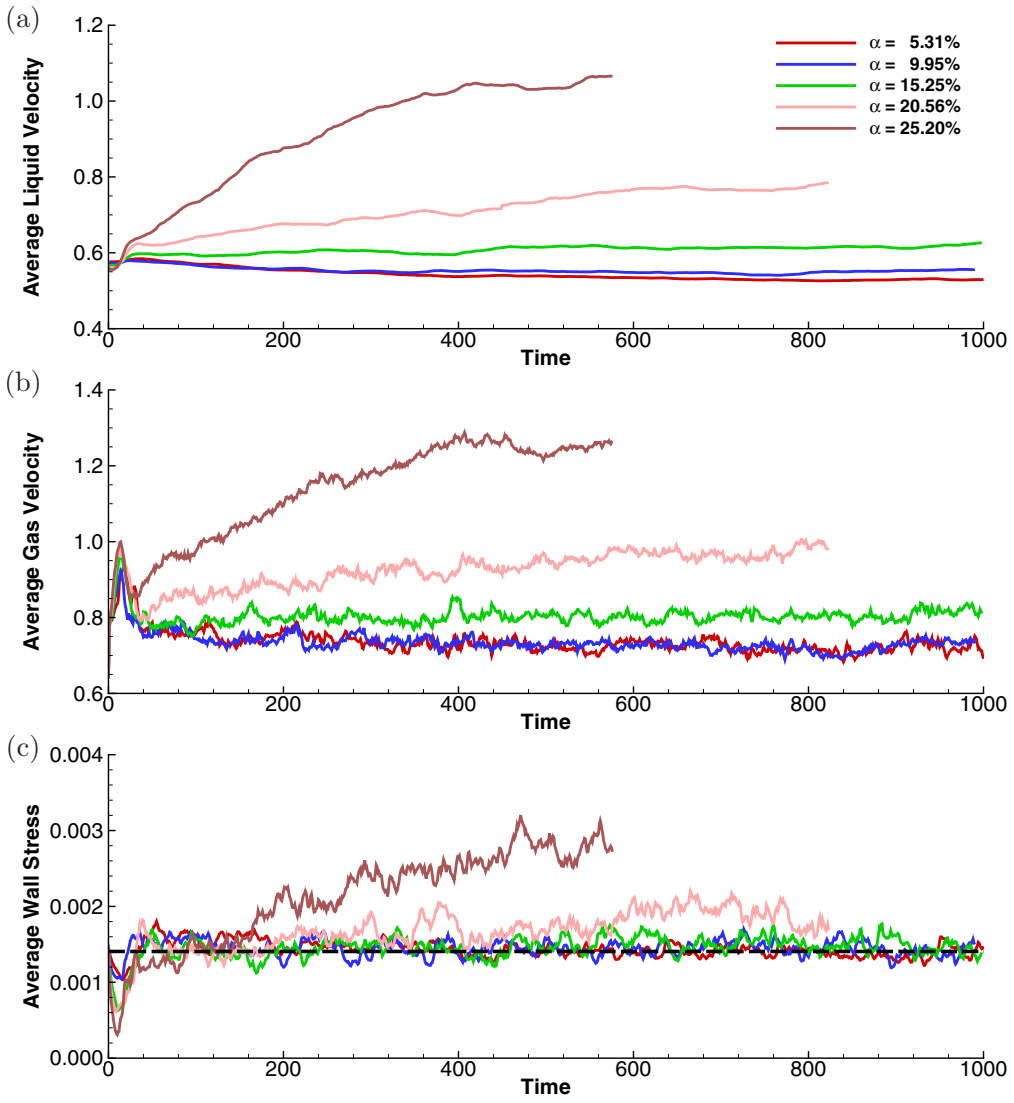

FIG. 2. (a) The liquid velocity; (b) the gas velocity; (c) the wall shear stress, versus time for all five cases. The dashed line in panel (c) is the equivalent wall shear stress balanced by β.

have remained near the steady state for most of the simulations, but the two higher void fraction cases have a long transient that has not fully disappeared.

In Fig. 3 we examine the surface area versus time. Instead of plotting the surface area directly, we compute the Sauter mean diameter (SMD) and the equivalent number of bubbles, from the total surface area and the volume occupied by the light fluid. We assume that the gas is contained in n bubbles of diameter d and use that the gas volume is then $V = n(\pi/6)d^3$ and the total surface area is $A = n\pi d^2$. Given V and A, we can solve for $d = 6(V/A)$ and $n = (1/36\pi)A^3/V^2$.[1] The top frame

[1] In our earlier paper on this subject [28], the equation in the text on page 11 for the number of bubbles is wrong. However, as far as we can tell, Fig. 9 (bottom) in Ref. [28] is correct.

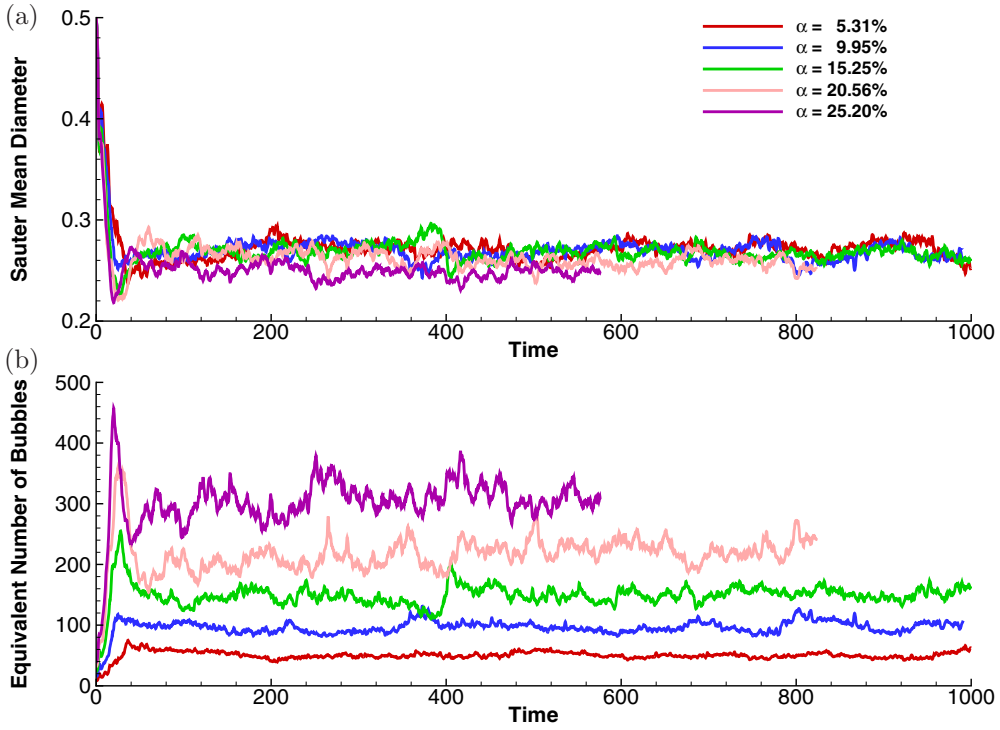

FIG. 3. (a) The Sauter mean diameter; (b) the equivalent number of bubbles versus time for all five cases.

shows that the SMD quickly settles down to a constant but fluctuating value and that the value is very similar for all cases, except for highest void fraction where it is slightly lower—although not by much. The observed diameter, $d_{\mathrm{SMD}} \approx 0.26$, corresponds to Eötvös number $\mathrm{Eo}_{\mathrm{SMD}} = 3.04$. The bottom frame shows that the number of equivalent bubbles increases with the void fraction, as we expect. The results of Figs. 2 and 3 suggest that the three lowest void fraction cases are very similar in that they quickly reach a well-defined stationary state where the gas and the liquid velocities (and thus the slip velocity) are similar and the bubble sizes are similar. The void fractions are different and therefore the number of bubbles. These cases are therefore clearly in the bubbly flow regime. The higher void fraction cases have similarly sized bubbles which appear to quickly settle down to a relatively stable distribution (at least as measured by the SMD) but take a much longer time to reach a steady state.

We have also done a simulation in Case 6 with the same void fraction as Case 1, but starting with the light fluid contained in many more smaller bubbles, as listed in Table I. After an initial short transient the evolution is in all aspects the same as for Case 1. Figure 4 shows the phase distribution at time 800, for the regular initial conditions (Case 1) on the left and the smaller initial bubbles (Case 6) on the right. We have compared the phase distribution at other times, as well as the wall shear, the flow rate, the surface area, and other quantities and find excellent agreement. Thus, we believe that the results presented here, and most definitely the long-time results, are independent of the specific initial conditions that we used for the phase distribution.

B. Long-time statistics

The focus of the present paper is on the nearly statistically stationary long-term state, and with the exception of the three figures discussed in the preceding section, we will not examine the transient evolution here. Although the two highest void fraction cases do not appear to have reached an exact

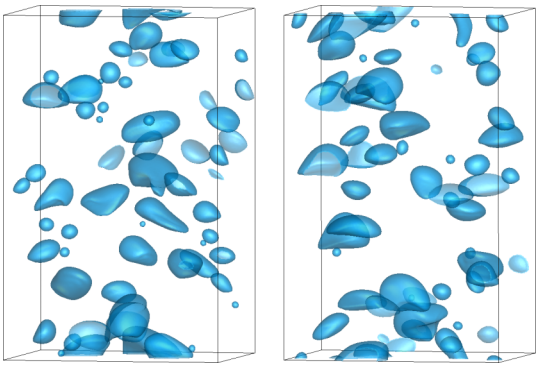

FIG. 4. The long-time state for different initial conditions. Left: regular initial bubbles (Case 1); right: small initial bubbles (Case 6).

stationary state, many aspects appears to have done so, so we will average over the latest times, as discussed below. Figure 5 shows the interface at a late time for the five different void fractions in the top row and contours of the streamwise velocity in the center plane in the bottom row, along with the interfaces of the bubbles crossing the plane. The lowest void fraction is on the left and the highest on the right. For the lowest void fraction the flow can clearly be classified as bubbly flow. The bubbles are smaller than the initial ones and come in a variety of sizes. The largest ones are highly deformed, but the smaller ones are nearly spherical. An examination of additional frames shows that although coalescence and breakup take place continually, the overall distribution of bubble sizes is relatively constant. As the void fraction is increased in the second frame, we see a larger number of bubbles, but the overall structure is not unlike the lowest void fraction case, so it is still reasonable to refer

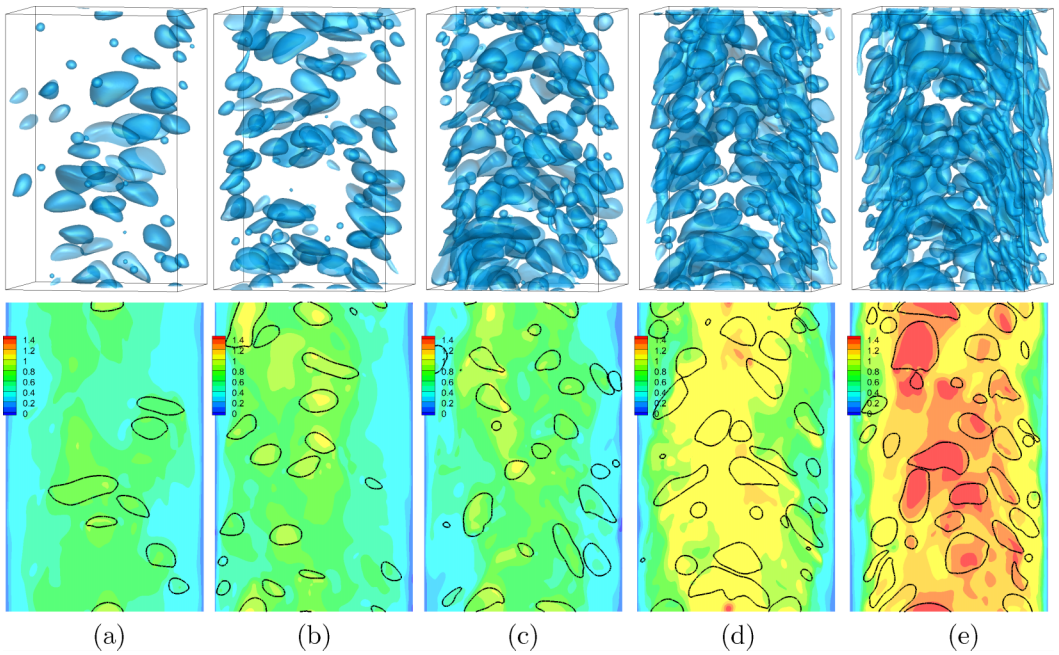

FIG. 5. The fluid interface at late times for all five cases in the top row and contours of the streamwise velocity in a plane through the middle of the channel in the bottom row.

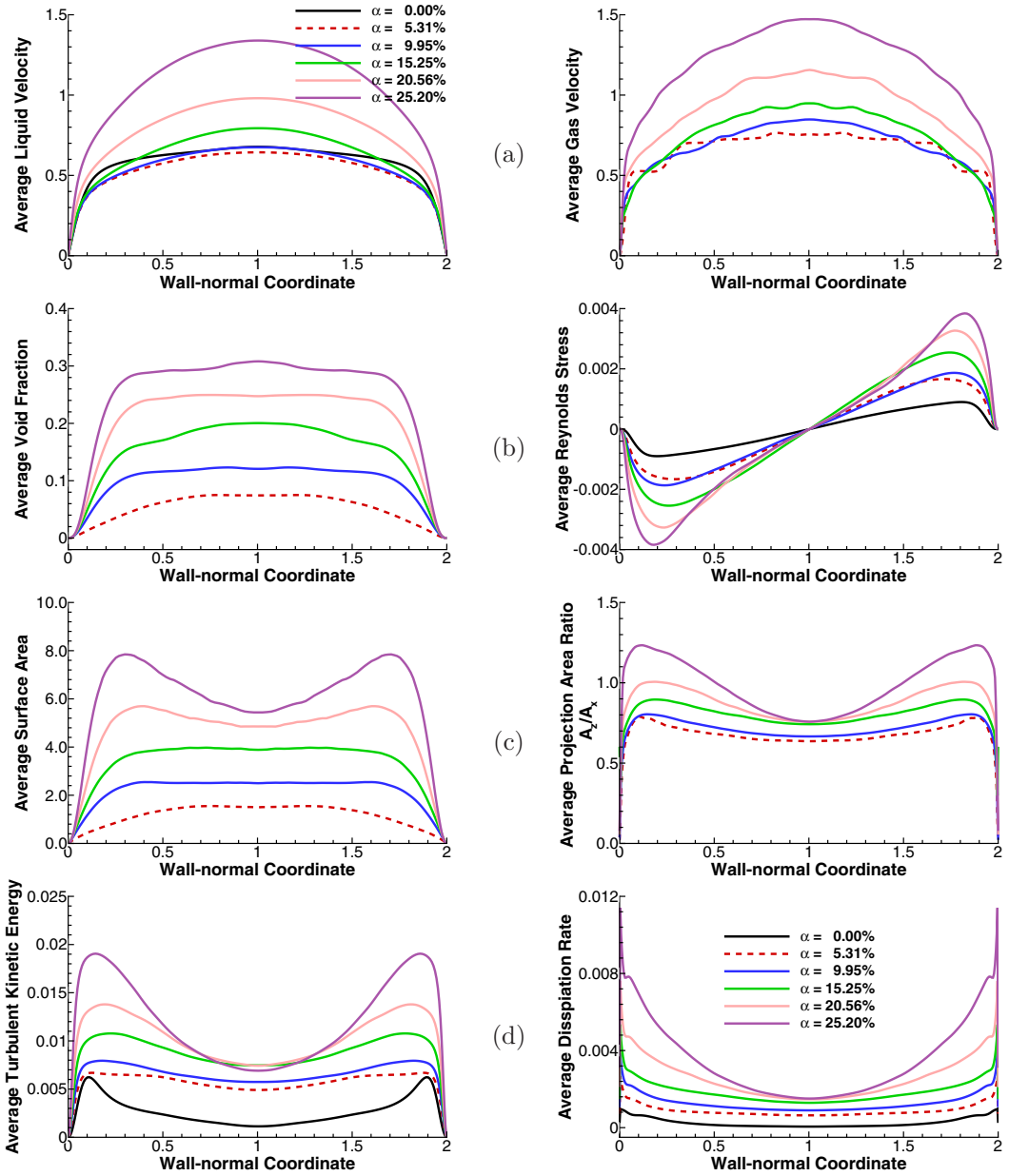

FIG. 6. Averaged profiles at nearly steady state for all five cases. (a) The liquid velocity (left) and the gas velocity (right). (b) The void fraction (left) and the Reynolds stresses (right). (c) The surface area (left) and the ratio of the projected area in the spanwise and the streamwise directions (right). (d) The turbulent kinetic energy (left) and the turbulent dissipation (right). The profiles are averaged over 500 time units for Cases 1, 2, and 3, but only over 100 time units for Cases 4 and 5.

to the flow as bubbly flow. For an even higher void fraction, in the middle frame, small bubbles are clearly visible, but many of the large interface structures are strongly deformed and barely bubbles in the usual sense. The change in interface structure continues as the void fraction increases. While small bubbles are still visible for the two large void fraction cases, the large fluid structures are

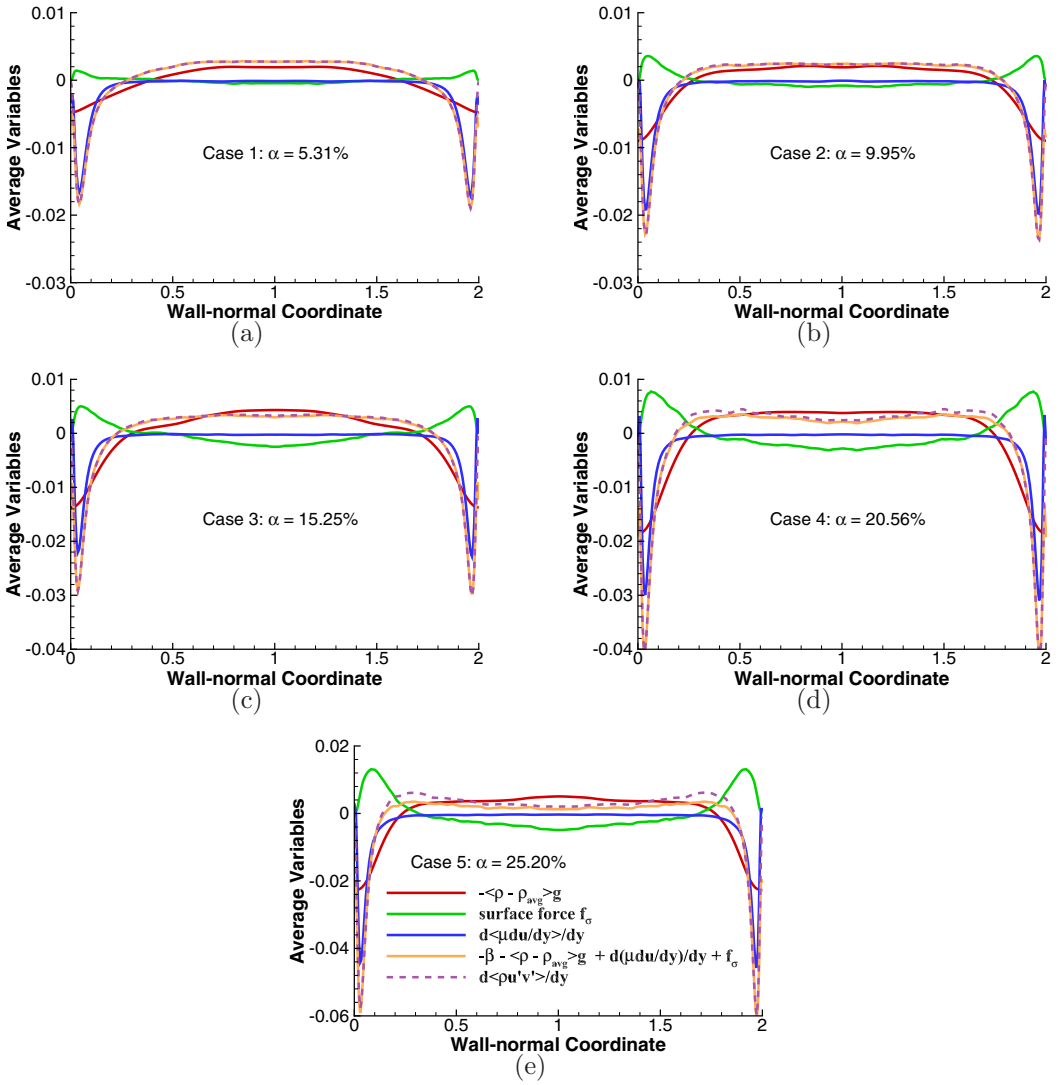

FIG. 7. The various terms of the average momentum balance [Eq. (3)] across the channel for all five cases. The averaging is done as in Fig. 6.

much more convoluted. The streamwise velocity is lowest at the walls in all cases, as expected, and increases in the middle of the channel as the void fraction increases. For the highest void fraction case it is, in particular, clear that the velocity in the core shows large fluctuations. For the lower void fractions the velocity in the bubbles is not significantly higher than in the liquid, since the slip velocity is relatively modest compared to the bulk velocity.

Profiles of several quantities averaged over planes parallel to the walls, after the flow has reached an approximately steady state, are shown in Fig. 6. Since the three lowest void fraction cases clearly have reached steady state, we average over long times, from time 500 to 1000, for those, but only for the last 100 time units for the two higher void fraction cases. Where relevant, we include the profile for single-phase flow ($\alpha = 0\%$) for reference. The average liquid (left) and the gas (right) velocities are shown in the top row. For the two lowest void fractions the liquid velocities are nearly the same, and fairly close to the velocity for single-phase flow, although the single-phase velocity is slightly

FIG. 8. One example of the interface structure at early time for Case 3.

more uniform in the middle of the channel. The gas velocities are also similar. The velocities for Case 3 are higher but only slightly so. The velocities for the highest void fractions, on the other hand, are significantly larger, as well as more nonuniform. The second row shows the average void fraction on the left and the average Reynolds stresses in the liquid on the right. The shape of the void fraction profiles is similar in that the value in the middle of the channel is nearly constant, except for the lowest void fraction, and drops off sharply near the walls. The numerical values for the different cases are obviously not the same. The Reynolds stresses for the two lowest void fraction cases are nearly identical, but the slope is significantly larger than for single-phase flow, since the Reynolds stresses balance not just the pressure gradient but the buoyancy term also. For the higher void fractions both the slope in the center and the values close to the walls are larger. The third row shows the total surface area on the left and the ratio of the area projected in the spanwise and the streamwise directions on the right. The surface area obviously grows with void fraction and is highest in the center for the lowest void fraction, nearly uniform in the middle for the intermediate void fractions, and highest close to the walls for the highest void fractions. The higher surface area near the walls suggest that the bubbles there are more deformed than in the middle, since the void fraction is nearly constant. The ratio of the projected areas suggests that the bubbles are "flat" (or oblate ellipsoids) for the lower void fractions and in the middle of the channels for the higher ones, since the projection of the area in the horizontal direction is smaller than the projection in the vertical streamwise direction. The higher ratios near the walls, for the highest void fractions, are presumably a result of the streamwise filaments or tilted deformed bubbles, seen in the rightmost frame in Fig. 5. The turbulent kinetic energy (left) and the turbulent dissipation (right) in the liquid are shown in the

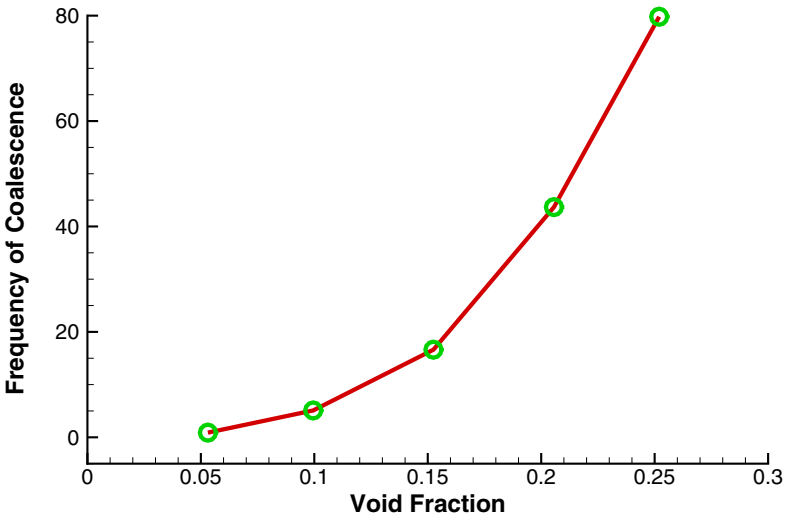

FIG. 9. The frequency of coalescence versus void fraction at steady state.

bottom row. For all void fractions the kinetic energy drops to zero at the walls but the dissipations spikes, as expected. For the lowest void fraction the profiles are, again, similar and uniform across most of the channel. Both the kinetic energy and the dissipation are significantly higher than for single-phase flow, and as the void fraction increases the values for both in the middle of the channel remain similar to the low void fraction cases (although slightly larger) but the values near the walls grow.

Averaging Eq. (1) over planes parallel to the walls, over both fluids, gives

$$\frac{\partial \rho U}{\partial t} = -\beta - \langle(\rho - \rho_{avg})g\rangle + \frac{d}{dy}\left\langle \mu \frac{du}{dy} \right\rangle - \frac{d}{dy}\langle \rho u' v' \rangle + \left\langle \sigma \int_F \kappa_f \mathbf{n}_f \delta(\mathbf{x} - \mathbf{x}_f)\, dA_f \right\rangle, \quad (3)$$

for $U(y)$, the average velocity in the vertical direction. Here the brackets, $\langle\ \rangle$, denote the averages. The second to fifth terms on the right-hand side are the buoyancy force, the viscous stress, the Reynolds stress, and the surface force, respectively. At steady state the left-hand side is zero. For single-phase flow the gravity and surface tension terms are zero so $\beta = d\tau_T/dy$, where τ_T is the sum of the viscous and the Reynolds stresses. For spherical clean bubbles the average surface force is zero, and the lift forces move the bubbles in such a way that the gravity term balances β in the middle of the channel [8,10]. This leads to considerable simplifications, and the void fraction profile can be approximated analytically. In our case, however, there is no reason to believe that any of the terms on the right-hand side will be zero. Figure 7 shows the various terms—and sums of terms—in Eq. (3) at late times for all five cases. We first note that in the middle of the channel the viscous stresses are essentially zero for all the cases, and the balance is predominantly between the buoyancy term and the Reynolds stresses. Only for the lowest void fraction case does the imposed pressure gradient add a slight amount. Second, in the middle of the channel the surface force is nearly zero for the lowest void fraction but then becomes increasingly negative. Near the wall it changes sign and increases with void fraction. At the wall the buoyancy changes sign, since no light fluid is there, and the viscous stresses increase significantly. The Reynolds stresses increase also, and the main balance continues to be between the Reynolds stresses and the rest of the terms on the right-hand side of Eq. (3). Notice that the terms add up to nearly zero, even for the highest void fractions where the flow is still slowly slowing down, emphasizing how slowly the velocity is going down. We have examined a large number of other quantities, such as velocity fluctuations and vorticity, and generally find that those are very similar for the lowest void fractions and are more

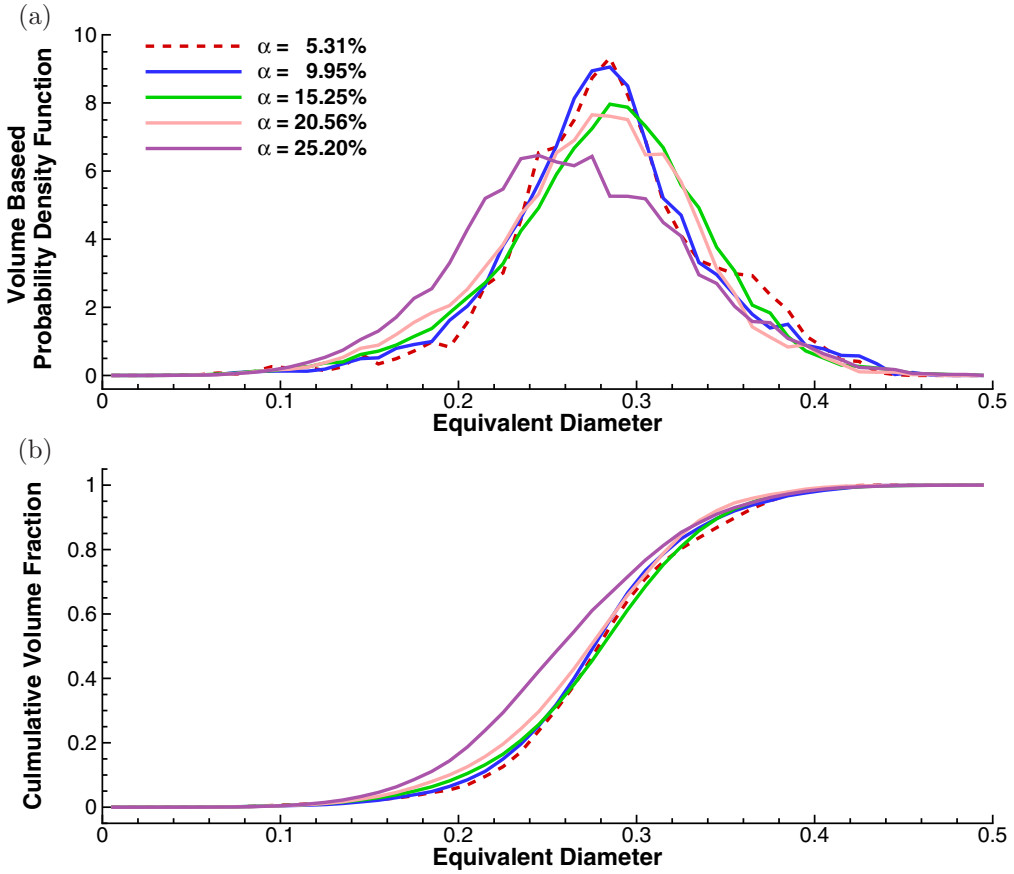

FIG. 10. The probability distribution of blob sizes of the light fluid for all cases. (a) The volume-based probability density function and (b) the cumulative volume fraction, at nearly steady state.

or less uniform across most of the channel, but increase for higher void fractions and have a peak near the walls. The plots in Figs. 5–7 show that the overall flow structure remains similar as the void fraction increases, but the flow rate increases. We note that we are keeping the driving force [β in Eqs. (1) and (3)] constant, so when the mixture becomes lighter, we reduce the pressure gradient.

For the lowest void fraction case it is clear that the light fluid consists of discrete and well-defined bubbles. For the higher void fractions the geometry of the regions occupied by the light fluid is more complex. In Fig. 8 we show the blobs at an early time for Case 3. Each blob is colored differently, and we have made all but one semitransparent to make other blobs visible. The nontransparent blob, shown in red, is highly convoluted and is likely to undergo changes in its topology in the near future. It is also unlikely that its motion can be described assuming that it is a "regular" bubble. We note that some of the blobs extend across the periodic boundaries and should, in principle, be cut and a part placed on the other side of the computational domain. We have not done so to emphasize their connectivity.

The average frequency of coalescence is shown in Fig. 9, for a late time interval. The averaging is over shorter time than most of the data presented here since we did not record when topology change took place for the earlier times and did not have a way to reconstruct the information from the data collected during the run. We have, however, confirmed that the results are reasonably well converged in the sense that the data do not depend on the length of the time interval. As expected, the frequency of topology changes remains low for the lowest void fractions, but then grows rapidly as the void

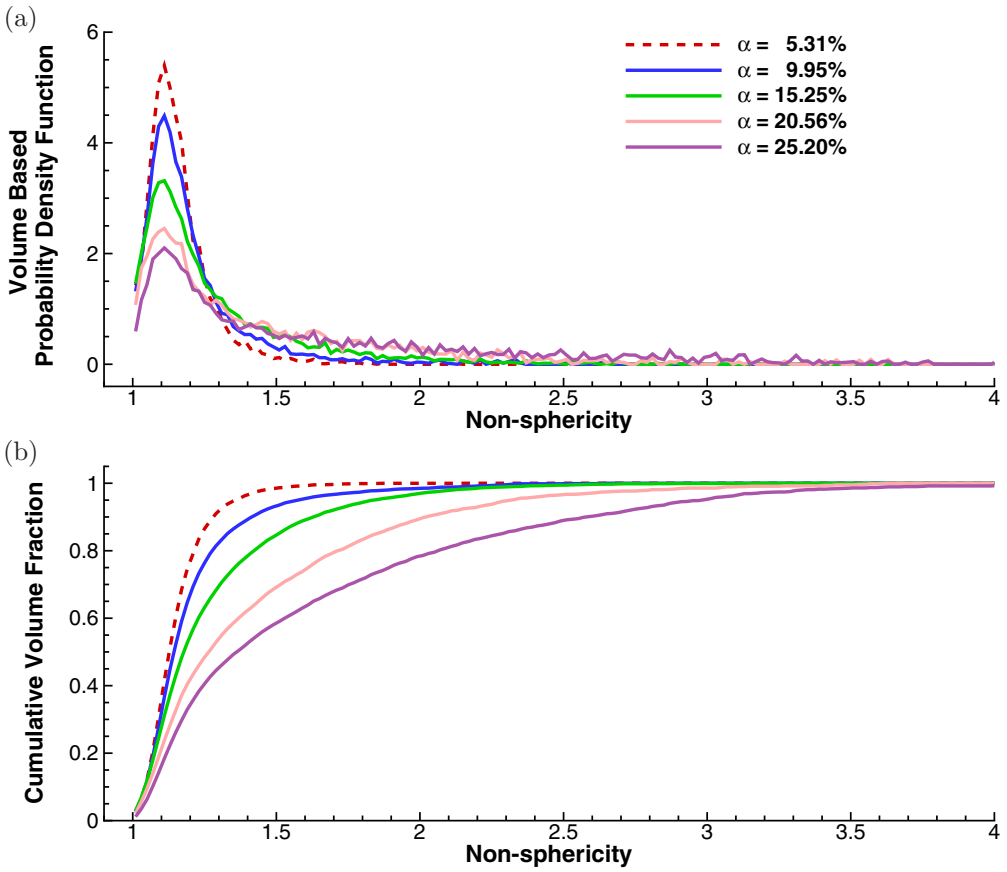

FIG. 11. The probability distribution of the light fluid blobs' nonsphericity for all cases. (a) The volume-based probability density function and (b) the cumulative volume fraction, at nearly steady state.

fraction increases. We have also computed the frequency of breakups and find that they agree well with the frequency of coalescence at low void fractions. For statistically steady state, where the number of blobs of the light fluid remain constant on the average, this is what we expect. However, under some complex situations at higher void fractions, where multiple breakups of the same blob can take place at the same time and breakups do not always lead to separate blobs, we could not identify what was a distinct breakup, and therefore the numbers of breakups and coalescences did not always match.

To quantify the distribution of flow structures and, in particular, to assess if it makes sense to talk about bubbles for the higher void fractions, we have found all blobs containing light fluid, by identifying connected interfaces, at several times for each case and computed their volume and surface area. Figure 10 shows the probability distribution of blob sizes for all five cases, where the equivalent diameter d_{eqv} is found by assuming that the volume of each blob is contained in a sphere with diameter d_{eqv}. The probability density function (PDF), which is calculated as the fractional volume of each blob size, is plotted in the top frame and the cumulative distribution in the bottom frame. Obviously, very little of the light fluid is contained in bubbles with an equivalent diameter less than about 0.2, about half of the volume is contained in blobs with an equivalent diameter of 0.28 (and $\mathrm{Eo}_{d=0.28} = 3.5$), and almost all the volume is in blobs with a diameter of 0.4 or less. Notice that although the mean equivalent diameter for the blobs containing most of the light fluid is about the same as the SMD in Fig. 3, they are different. What Fig. 10 does show,

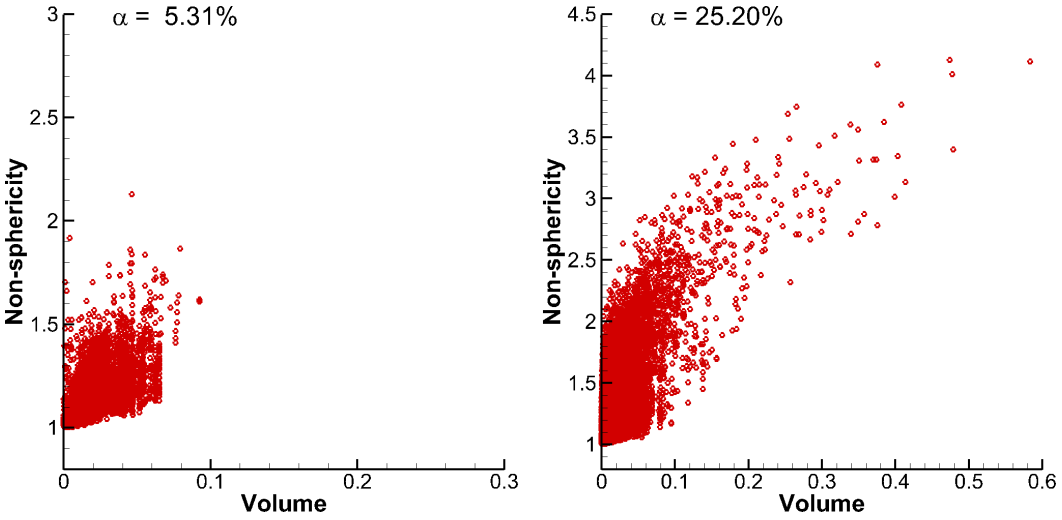

FIG. 12. The nonsphericity of each blob versus its volume, as a scatter plot, for the lowest void fraction (left) and the highest void fraction (right).

however, is that the distribution of equivalent diameters is similar for all the cases, just as the SMD was approximately the same. The highest void fraction case has slightly smaller bubbles, which is consistent with Fig. 3. As discussed later (Fig. 15), we have also compared the number of blobs to the numbers in Fig. 3 and find that for the lowest void fraction cases, where the light fluid consists of

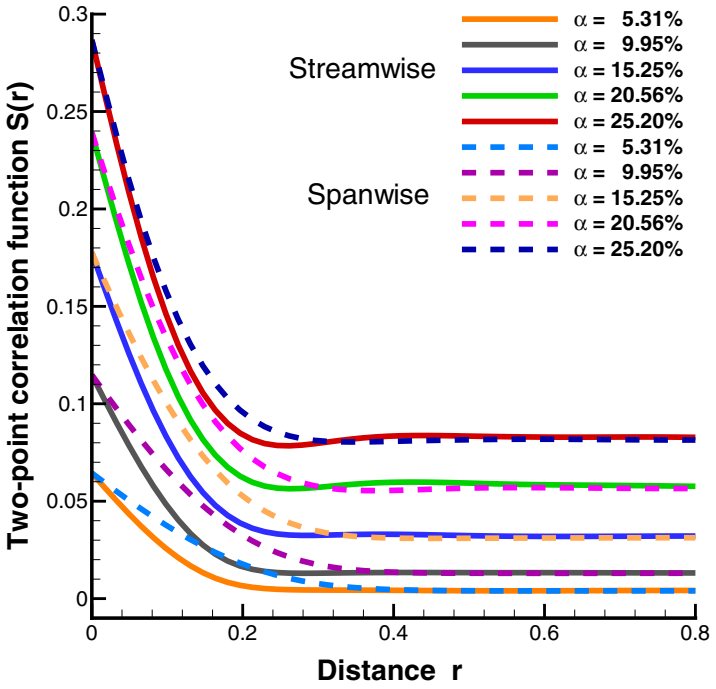

FIG. 13. The two-point probability function for the phase distribution in the streamwise (solid line) and the spanwise (dashed line) directions.

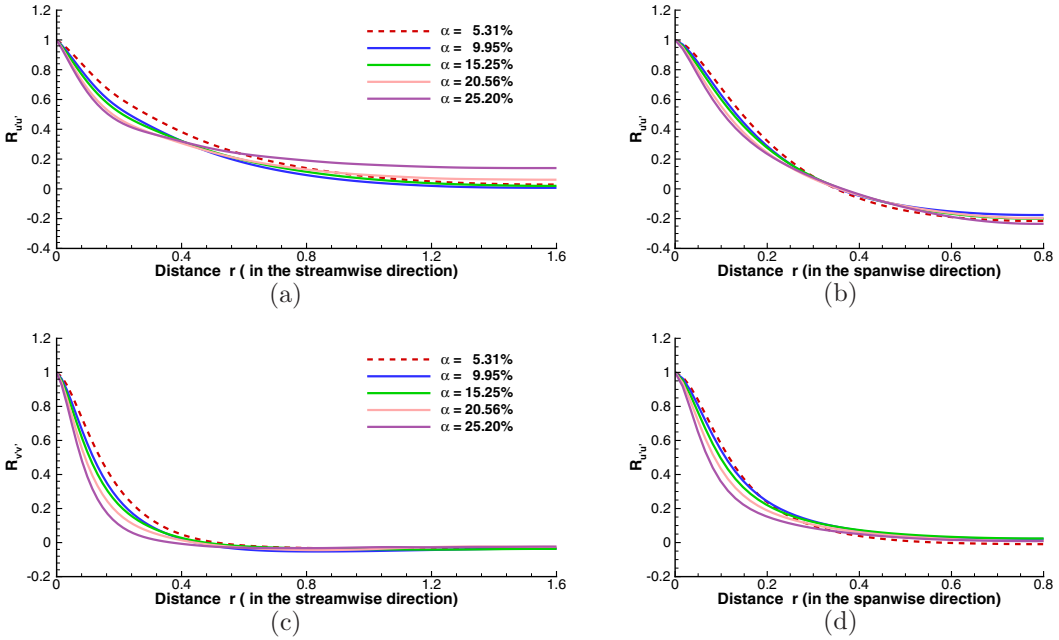

FIG. 14. The velocity conditional correlation functions. (a) $R_{u'u'}$ in the streamwise direction; (b) $R_{u'u'}$ in the wall-normal direction; (c) $R_{v'v'}$ in the streamwise direction; (d) $R_{v'v'}$ in the wall-normal direction.

well-defined bubbles, the numbers are similar, but at the higher void fraction where there are large irregularly shaped blobs, the actual number of blobs is much smaller than the equivalent number in Fig. 3. Since a highly convoluted blob is likely to be better approximated by several smaller small spherical bubbles, rather than one large one, this seems reasonable.

We have also computed the "nonsphericity" of each blob by dividing the surface area by the surface area of a sphere with the corresponding volume. Since a sphere has the smallest surface area for a given volume, this ratio is obviously always larger than unity. The PDF is plotted in the top frame of Fig. 11 versus the nonsphericity for all five cases and the cumulative distribution in the bottom frame. The PDF peaks for low nonsphericity, and the cumulative volume grows very quickly with increasing nonsphericity, but the height of the peak of the PDF and the growth of the nonsphericity depends strongly on the void fraction. For the lowest void fraction case almost all the volume is contained in blobs with nonsphericity less or equal to 1.5, but for the highest void fraction not all the volume is accounted for when the nonsphericity is equal to 3.0. We note for reference that the nonsphericity of an oblate ellipsoid with a thickness of one-fourth of the diameter is 1.44, so it seems unlikely that we can talk about distinct bubbles for nonsphericity higher than 2 or so. Thus, the figure suggests that at best the lowest three volume fractions can be considered "real" bubbly flows.

To gain a better insight into the distribution of bubble sizes and shapes, we show a scatter plot of the nonsphericity of each light fluid blob versus its volume, in Fig. 12, for 500 late times for the lowest void fraction, and 100 late times for the highest void fraction. For the low void fraction case essentially all the blobs are small and the nonsphericity is mostly below 1.5, but for the larger void fraction the nonsphericity is much larger, even for the small blobs, and there is a scattering of blobs that are very large and have large nonsphericity. We have not included the intermediate void fractions since they fall in between the extreme cases. We have also plotted the nonsphericity versus surface area (not shown) and find, not unexpectedly, that those follow each other, although with some scatter.

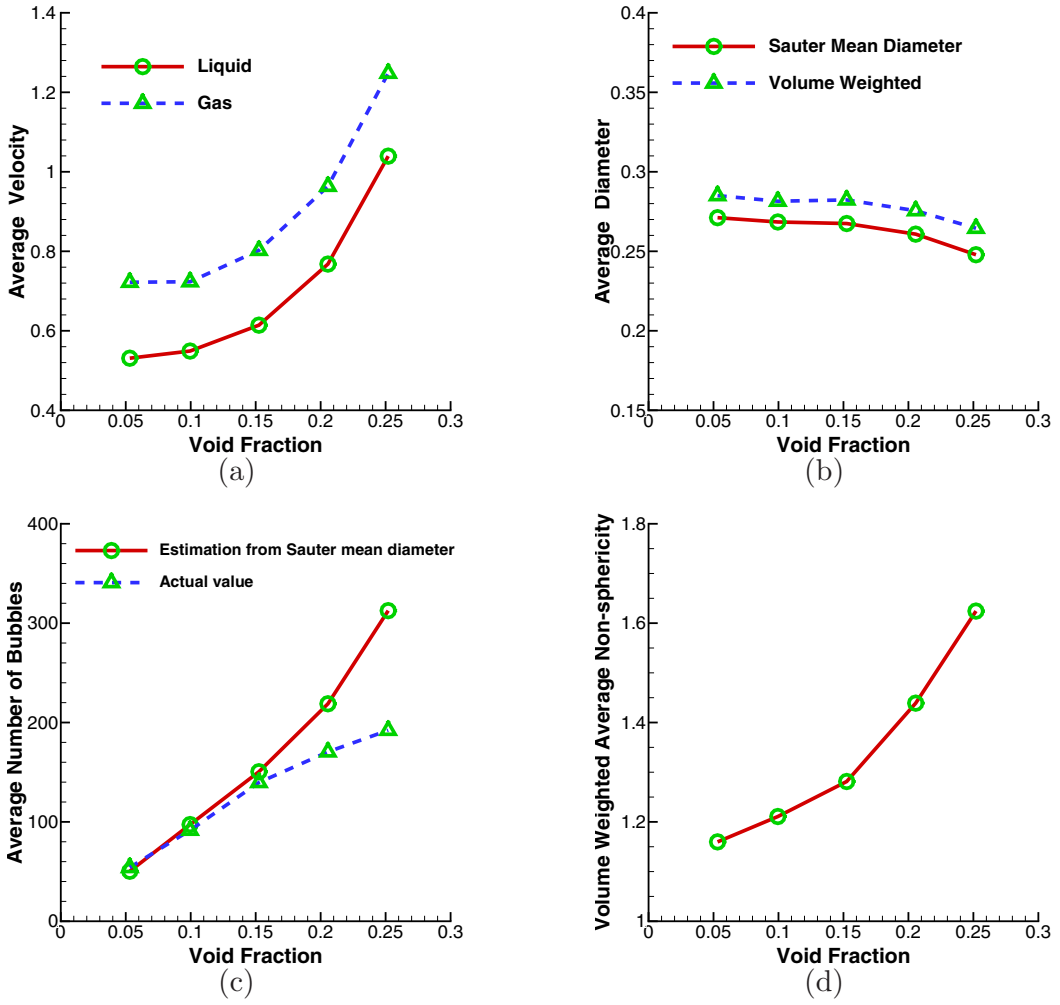

FIG. 15. Averages over the whole domain versus void fraction, at statistically steady state. (a) The average velocities of the heavy (liquid) and the light (gas) fluid; (b) the SMD and the volume-weighted diameter of blobs of the light fluid; (c) the number of blobs of the light fluid as well as the SMD estimate; (d) the volume-weighted nonsphericity.

To examine the phase distribution we plot the two-point correlations for the light fluid in Fig. 13, for both the streamwise and spanwise directions. We define an indicator function χ such that $\chi = 1$ in one fluid and $\chi = 0$ in the other one. The two-point correlation function for the $\chi = 1$ fluid is then defined by

$$S_2(r) = \langle \chi(\mathbf{x})\chi(\mathbf{x}+\mathbf{r})\rangle, \tag{4}$$

where the brackets $\langle\ \rangle$ denote the appropriate average. Obviously $\chi(\mathbf{x})\chi(\mathbf{x}+\mathbf{r}) = 1$ if $\mathbf{x}$ and $\mathbf{x}+\mathbf{r}$ are both in the same fluid where $\chi = 1$, but zero if one or both points are in the other fluid. The correlation drops off relatively rapidly, and although the spanwise correlation drops slightly faster, at a distance of 0.3 or so the phase distribution is essentially uncorrelated.

Figure 14 shows the conditional correlation between the fluctuation velocity at two different points in the same fluid, computed by

$$R_{ij} = \frac{\langle \chi(\mathbf{x}) u_i'(\mathbf{x}) \chi(\mathbf{x}+\mathbf{r}) u_j'(\mathbf{x}+\mathbf{r}) \rangle}{\langle \chi(\mathbf{x}) u_i'(\mathbf{x}) u_j'(\mathbf{x}). \rangle}. \tag{5}$$

Here $i, j = 1$, 2, or 3, for the streamwise, wall-normal, and spanwise directions, and we divided by the single-point correlation to obtain a value of unity for $\mathbf{r} = 0$. The streamwise correlations are shown on the left and the spanwise on the right. The spanwise correlation of the streamwise velocity fluctuations, $\langle u'u' \rangle$, is shown in the top row, and the spanwise correlation of velocity fluctuations in the wall-normal direction, $\langle v'v' \rangle$, in the bottom row. The $\langle v'v' \rangle$ correlations are both nearly zero for a distance of about 0.4, but the $\langle u'u' \rangle$ correlations decay slower. Other velocity correlations show similar behavior. A comparison of Figs. 13 and 14 shows that the velocity is correlated over larger distances than the phase distribution. The correlations for both the phase distribution and the velocity are computed for the middle of the channel, from $y = 0.3$ to $y = 1.7$, for all cases.

A few quantities averaged over the whole channel, and plotted versus the void fraction in Fig. 15, summarize some of the results discussed here. In Fig. 15(a) we show that the average gas and the liquid velocities both increase rapidly with void fraction, but the slip velocity remains nearly constant. The average equivalent diameter of blobs of the lighter fluid, shown in Fig. 15(b), computed either as the average of the equivalent diameters of each blob or as the SMD, is nearly constant and decreases only slightly as the void fraction increases. The average number of blobs, found either by counting the number of connected blobs or as an equivalent number when finding the SMD, is shown in Fig. 15(c). Both increase with the void fraction, but whereas the different estimates agree for low void fractions, at higher void fractions the real number of blobs grows more slowly than the SMD estimate. This is consistent with the average nonsphericity, shown in Fig. 15(d) of blobs of the light fluid, which grows as the void fraction increases and highly contorted blobs become more common.

V. CONCLUSIONS

We have examined the effect of the void fraction on the structure of multiphase flow in a vertical channel where the surface tension has been taken to be sufficiently low so that the interface continuously undergoes coalescence and breakup. We find that at modest void fraction the overall structure of the flows remains similar as the void fraction changes and the flow can be characterized as a bubbly flow. As the void fraction increases beyond approximately 10%–15% the structure starts to change, although the light fluid continues to be contained in distinct blobs. It is perhaps slightly surprising, but the distribution of blob sizes remains essentially the same for all void fractions, with the exception that for the highest void fraction case a shift to slightly smaller blobs is seen. The main difference is that as the void fraction increases the blobs are more deformed and the surface area larger. Even when the total forcing of the flow, the imposed pressure gradient plus the mixture weight, is kept constant, the flow rate increases as the void fraction increases. The slip velocity remains, however, essentially constant. We emphasize that although we have computed averages at late times for the two highest void fraction cases, the wall shear has not reached its equilibrium value, and the flow is therefore still slowing down, although very slowly. Thus, the results for those two cases are only approximations to what to expect at truly stationary states. We do not, however, expect the overall conclusions for those void fractions will change much at longer times. We note that although we clearly have bubbly flows at low void fractions the nonbubbly state could consist of several different regimes. This remains to be studied in more detail.

We have avoided referring to the simulations presented here as DNS since the term usually refers to verified solution of a validated mathematical model, for systems containing a large range of temporal and spatial scales. While our system contains a large range of scales, fully verified solutions are accurate solutions of the governing equations, independent of any numerical parameters such as grid resolution, and a validated model requires the equations to capture faithfully

the physical processes that we are simulating. For our case those are only approximately satisfied. The smallest scale structures are likely to be under-resolved, and the physical processes responsible for the actual rupture of thin films are approximated in a crude way. These are the same challenges faced in simulations of atomization and breakup [41–46]. Most of those simulations are, however, done advecting the marker function directly on the fluid grid, using VOF or level set methods, where topology changes always take place for structures on the grid scale, in an uncontrolled way. It has been known for a long time that explicit tracking of the interface maintains the integrity of the interface better [47], and we hope, in particular, that the small-scale surface forces are captured more accurately.

The characterization of complex multiphase flows undergoing rapid topology changes is a challenging topic, and we note that we sought ideas from many fields for the appropriate strategies, including from studies of random heterogeneous materials [48] and the dynamic evolution of interfaces undergoing mixing in rheology and turbulent combustion [49–51]. As we move further toward developing the insight and the data needed to improve average two-fluid and LES-like models, we are likely to need to draw on those sources even further.

ACKNOWLEDGMENTS

This research was supported by the Consortium for Advanced Simulation of Light Water Reactors, an Energy Innovation Hub for Modeling and Simulation of Nuclear Reactors under U.S. Department of Energy Contract No. DE-AC05-00OR22725. We also acknowledge the use of computational resources at the Maryland Advanced Research Computing Center (MARCC).

[1] I. A. Bolotnov, K. E. Jansen, D. A. Drew, A. A. Oberai, R. T. Lahey, and M. Z. Podowski, Detached direct numerical simulations of turbulent two-phase bubbly channel flow, Int. J. Multiphase Flow **37**, 647 (2011).

[2] I. A. Bolotnov, R. T. Lahey, D. A. Drew, and K. E. Jansen, Turbulent cascade modeling of single and bubbly two-phase turbulent flows, Int. J. Multiphase Flow **34**, 1142 (2008).

[3] B. Bunner and G. Tryggvason, Effect of bubble deformation on the stability and properties of bubbly flows, J. Fluid Mech. **495**, 77 (2003).

[4] W. Dijkhuizen, I. Roghair, M. V. S. Annaland, and J. Kuipers, DNS of gas bubbles behavior using an improved 3D front tracking model—Drag force on isolated bubbles and comparison with experiments, Chem. Eng. Sci. **65**, 1415 (2010).

[5] W. Dijkhuizen, I. Roghair, M. V. S. Annaland, and J. Kuipers, DNS of gas bubbles behavior using an improved 3D front tracking model—Model development, Chem. Eng. Sci. **65**, 1427 (2010).

[6] A. Esmaeeli and G. Tryggvason, A DNS study of the buoyant rise of bubbles at O(100) Reynolds numbers, Phys. Fluids **17**, 093303 (2005).

[7] J. Lu and G. Tryggvason, Effect of bubble size in turbulent bubbly downflow in a vertical channel, Chem. Eng. Sci. **62**, 3008 (2007).

[8] J. Lu and G. Tryggvason, Dynamics of nearly spherical bubbles in a turbulent channel upflow, J. Fluid Mech. **732**, 166 (2013).

[9] M. van Sint Annaland, W. Dijkhuizen, N. Deen, and J. Kuipers, Numerical simulation of gas bubbles behavior using a 3D front tracking method, AIChE J. **52**, 99 (2006).

[10] G. Tryggvason and J. Lu, Direct numerical simulations of bubbly flows, Mech. Eng. Rev. **2**, 15 (2015).

[11] G. Tryggvason, M. Ma, and J. Lu, DNS assisted modeling of bubbly flows in vertical channels, Nucl. Sci. Eng. **184**, 312 (2016).

[12] S. Elghobashi, Direct numerical simulation of turbulent flows laden with droplets or bubbles, Ann. Rev. Fluid Mech. **51**, 217 (2019).

[13] B. Bois, Direct numerical simulation of a turbulent bubbly flow in a vertical channel: Towards an improved second-order Reynolds stress model, Nucl. Eng. Des. **321**, 92 (2017).

[14] X. Feng, C. Yang, Z.-S. Mao, J. Lu, and G. Tryggvason, Bubble induced turbulence model improved by direct numerical simulation of bubbly flow, Chem. Eng. J. (2018), doi:10.1016/j.cej.2018.09.162.
[15] B. Magolan, E. Baglietto, C. Brown, I. Bolotnov, G. Tryggvason, and J. Lu, Multiphase turbulence mechanisms identification from consistent analysis of direct numerical simulation data, Nucl. Eng. Technol. **49**, 1318 (2017).
[16] M. Ma, J. Lu, and G. Tryggvason, Using statistical learning to close two-fluid multiphase flow equations for a simple bubbly system, Phys. Fluids **27**, 092101 (2015).
[17] M. Ma, J. Lu, and G. Tryggvason, Using statistical learning to close two-fluid multiphase flow equations for bubbly flows in vertical channels, Int. J. Multiphase Flow **85**, 336 (2016).
[18] Z. Bilicki and J. Kestin, Transition criteria for two-phase flow patterns in vertical upward flow, Int. J. Multiphase Flow **13**, 283 (1987).
[19] Y. Taitel, D. Bornea, and A. E. Dukler, Modeling flow pattern transitions for steady upward gas-liquid flow in vertical tubes, AIChE J. **26**, 345 (1980).
[20] N. K. Tutu, Pressure fluctuations and flow pattern recognition in vertical two-phase gas-liquid flows, Int. J. Multiphase Flow **8**, 443 (1982).
[21] T. Yoshinaga and Y. Sato, Performance of an air-lift pump for conveying coarse particles, Int. J. Multiphase Flow **22**, 223 (1996).
[22] R. Rozenblit, M. Gurevich, Y. Lengel, and G. Hetsroni, Flow patterns and heat transfer in vertical upward air-water flow with surfactant, Int. J. Multiphase Flow **32**, 889 (2006).
[23] A. Manera, H.-M. Prasser, D. Lucas, and T. van der Hagen, Three-dimensional flow pattern visualization and bubble size distributions in stationary and transient upward flashing flow, Int. J. Multiphase Flow **32**, 996 (2006).
[24] G. F. Hewitt and D. N. Roberts, Studies of two-phase flow patterns by simultaneous x-rays and flash photography, Technical Report M-2159, Atomic Energy Research Establishment, Harwell, England (1969).
[25] G. B. Wallis, *One-Dimensional Two-Phase Flow* (McGraw-Hill, New York, 1969).
[26] V. C. Samaras and D. P. Margaris, Two-phase flow regime maps for air-lift pump vertical upward gas-liquid flow, Int. J. Multiphase Flow **31**, 757 (2005).
[27] S. Guet and G. Ooms, Fluid mechanical aspects of the gas-lift technique, Ann. Rev. Fluid Mech. **38**, 225 (2006).
[28] J. Lu and G. Tryggvason, Direct numerical simulations of multifluid flows in a vertical channel undergoing topology changes, Phys. Rev. Fluids **3**, 084401 (2018).
[29] R. D. Falgout and U. M. Yang, Hypre: A library of high performance preconditioners, in *Proceedings of the International Conference on Computational Science-Part III*, ICCS '02 (Springer-Verlag, Berlin, 2002), pp. 632–641.
[30] S. O. Unverdi and G. Tryggvason, A front-tracking method for viscous, incompressible, multi-fluid flows, J. Comput. Phys. **100**, 25 (1992).
[31] S. Biswas, A. Esmaeeli, and G. Tryggvason, Comparison of results from DNS of bubbly flows with a two-fluid model for two-dimensional laminar flows, Int. J. Multiphase Flow **31**, 1036 (2005).
[32] B. Bunner and G. Tryggvason, Dynamics of homogeneous bubbly flows: Part 1. Rise velocity and microstructure of the bubbles, J. Fluid Mech. **466**, 17 (2002).
[33] A. du Cluzeau, G. Bois, and A. Toutant, Analysis and modeling of reynolds stresses in turbulent bubbly up-flows from direct numerical simulations, J. Fluid Mech. **866**, 132 (2019).
[34] Y. Hao and A. Prosperetti, A numerical method for three-dimensional gas–liquid flow computations, J. Comput. Phys. **196**, 126 (2004).
[35] J. Hua and J. Lou, Numerical simulation of bubble rising in viscous liquid, J. Comput. Phys. **222**, 769 (2007).
[36] M. Muradoglu and A. D. Kayaalp, An auxiliary grid method for computations of multiphase flows in complex geometries, J. Comput. Phys. **214**, 858 (2006).
[37] J. F. Gibson, Channelflow: A spectral Navier-Stokes simulator in C++, Technical Report, University of New Hampshire, Channelflow.org (2014).

[38] J. F. Gibson, J. Halcrow, and P. Cvitanović, Visualizing the geometry of state space in plane Couette flow, J. Fluid Mech. **611**, 107 (2008).
[39] R. Clift, J. Grace, and M. Weber, *Bubbles, Drops, and Particles* (Academic Press, San Diego, 1978).
[40] S. Dabiri, J. Lu, and G. Tryggvason, Transition between regimes of a vertical channel bubbly upflow due to bubble deformability, Phys. Fluids **25**, 102110 (2013).
[41] G. M. Bianchi, P. Pelloni, S. Toninel, R. Scardovelli, A. Leboissetier, and S. Zaleski, Improving the knowledge of high-speed liquid jets atomization by using quasi-direct 3D simulation, in *7th International Conference on Engines for Automobile*, SAE Technical Paper 2005-24-089 (Consiglio Nazionale delle Ricerche, Italy, 2005).
[42] O. Desjardins and H. Pitsch, Detailed numerical investigation of turbulent atomization of liquid jets, Atomization Sprays **20**, 311 (2010).
[43] M. Herrmann, On simulating primary atomization using the refined level set grid method, Atomization Sprays **21**, 283 (2011).
[44] Y. Ling, D. Fuster, G. Tryggvason, and S. Zaleski, A two-phase mixing layer between parallel gas and liquid streams: Multiphase turbulence statistics and influence of interfacial instability, J. Fluid Mech. **859**, 268 (2019).
[45] T. Ménard, P.-A. Beau, S. Tanguy, F.-X. Demoulin, and A. Berlemont, Primary break-up: DNS of liquid jet to improve atomization modelling, in *Computational Methods in Multiphase Flow III* (WIT Press, Boston, 2005).
[46] J. Shinjo and A. Umemura, Simulation of liquid jet primary breakup: Dynamics of ligament and droplet formation, Int. J. Multiphase Flow **36**, 513 (2010).
[47] W. J. Rider and D. B. Kothe, Stretching and tearing interface tracking methods, AIAA Paper 95-1717 (1995).
[48] S. Torquato, Statistical description of microstructures, Ann. Rev. Mater. Res. **32**, 77 (2002).
[49] D. Lhuillier, Dynamics of interfaces and rheology of immiscible liquid-liquid mixtures, C. R. Mécanique **331**, 113 (2003).
[50] C. Morel, On the surface equations in two-phase flows and reacting single-phase flows, Int. J. Multiphase Flow **33**, 1045 (2007).
[51] E. Wetzel and C. Tucker III, Area tensors for modeling microstructure during laminar liquid-liquid mixing, Int. J. Multiphase Flow **25**, 35 (1999).